Characterization Progress of an Absorption Laser Differential Interferometer

Joshua M. Weisberger*, Brett F. Bathel†, and Gregory C. Herring‡
NASA Langley Research Center, Hampton, VA, 23681

An absorption laser differential interferometer (A-LDI) system can be used to provide simultaneous, colinear measurements of flow properties (pressure, temperature, concentration, velocity) and flow fluctuations. Further characterization work on the absorption aspect of the system is provided in this paper, including characterization of the laser operating parameters, comparisons of two etalons of different free spectral range, and the further evaluation of a fixed-wavelength absorption measurement that can be used to obtain absorption and LDI measurements with the same sampling rate. A 0.4 GHz etalon was demonstrated to provide sufficient fringe peaks at low modulation depths to be used for the low-pressure testing characteristic of hypersonic wind tunnel facilities. The use of a 3 GHz etalon as a low-cost relative wavemeter was tested and validated. Data taken with the fixed-wavelength strategy in a sub-atmospheric test cell using 100% O_2 was successful. This will allow absorption and LDI data to be acquired colinearly at the same sampling rate, yielding a truly simultaneous measurement of flow density fluctuations and mean density.

I. Introduction

Interferometric measurement techniques are often used in ground test facilities to make measurements of small fluctuations of index of refraction in a flow of interest. Their high sensitivity to small changes in index of refraction, and thus density [1], makes interferometric techniques particularly suitable for hypersonic wind tunnel and high-speed combustion (e.g., scramjet) facility measurements, both to characterize the freestream flow state and the flow around various test articles. A laser differential interferometer (LDI), developed in the 1970s [2–4], measures the difference in optical path length between two closely spaced parallel beams, and is equally sensitive to the index of refraction difference over the entire separated beam path length. In recent years, focusing LDI (FLDI) has been used extensively as a diagnostic due to its ability to reject unwanted signal from regions outside the flow of interest (e.g., wind tunnel wall/window boundary layers), and has been used for freestream flow characterization [5–9], boundary layer transition measurements [10–20], and turbulent jet measurements [21–24]. Work to quantify the density disturbance spectra from the FLDI measurements and to characterize the optical system's operation has been ongoing [25–31]. While LDI and FLDI measured data can be converted to a phase shift between the probing beams, and then to a relative fluctuating density, grounding these measurements to fundamental properties of the flow (temperature, pressure, density, etc.) remains challenging.

Absorption spectroscopy is a robust measurement technique that has a rich history of measuring various gas properties in the gas process industry, atmospheric remote sensing, wind tunnel measurements, shock tube measurements, combustion applications, and more [32, 33]. This technique is a simple method for simultaneous measurement of many gas properties using a single laser; the temperature, pressure, concentration, and velocity of a flow can be simultaneously obtained. Absorption spectroscopy has also found widespread use in the hypersonic testing community, particularly in characterizing the freestream state of wind tunnel facilities [6]. The molecular oxygen A-band absorption spectrum near 760 nm has been extensively used for O_2 property measurements in the past [34–50] where lasers and optics have become widely available. With sufficient absorption signal strengths, the simple direct absorption spectroscopy (DAS) measurement technique can be utilized. In DAS measurements that suffer from low absorption, wavelength modulation spectroscopy (WMS) can be employed to increase the signal-to-noise ratio (SNR)[51].

In a recently-published conference paper [52], an absorption laser differential interferometer (A-LDI) system was introduced to make simultaneous and colinear measurements of mean flow properties and flow fluctuations. The system

*Research Engineer, Advanced Measurements and Data Systems Branch, AIAA Senior Member.
†Research Engineer, Advanced Measurements and Data Systems Branch, AIAA Senior Member.
‡Research Engineer, Advanced Measurements and Data Systems Branch.

uses a tunable laser diode centered at 760 nm to probe the A-band absorption features of molecular oxygen, O_2. The decision to probe O_2 was made because most of the wind tunnels at NASA Langley Research Center (LaRC) use dried, compressed air, thus eliminating the need for seeding of the flow with a different absorbing gas [53]. Measurements were made in both a laboratory sub-atmospheric pressure-controlled test cell, as well as at the Probe Calibration Tunnel (PCT) at LaRC. Operation of the absorption and LDI aspects of the system were first independently verified, and then tested in a simultaneous measurement system. Absorption results from direct absorption spectroscopy (DAS) and wavelength modulation spectroscopy (WMS) were both promising. It was also demonstrated that constant-current absorption measurements with the laser tuned to the center of an absorption peak could prove useful for high-bandwidth measurements for comparison with LDI data.

This paper continues the development of the A-LDI system, which is described in Section II. Operation of the laser is discussed in Section III, including a characterization of the laser wavelength operating bounds, the slow-scan and modulation frequencies for WMS measurements, and the minimum required sampling rate. The use of a new, longer etalon for lower-pressure measurements is evaluated in Section IV, with comparisons to the old, shorter etalon used in Ref. [52]. The use of these two etalons as a means to make fixed-wavelength absorption measurements is explored in Section VI.

II. Experimental Setup

A schematic of the non-focusing A-LDI system is shown in Fig. 1, where the LDI aspect of the system follows the general design of Smeets and George [2–4]. The *pitch* (transmitting) side of the system is shown on the left, while the *catch* (receiving) side of the system is shown on the right. The optics on both sides are rigidly mounted to independent optical breadboards and are purged with N_2 gas to eliminate absorption of the laser light outside of the region-of-interest, where the black dashed lines denote the purged enclosures. A laser diode driver, LDD (Thorlabs, LDC205C), and temperature controller, TEC (Thorlabs, TED200C), are connected to a 760 nm tunable diode laser, TDL (Nanoplus GmbH), which is housed in a heat sink unit with a collimation optic for the beam output. An arbitrary function generator, Fnc. Gen. (Tektronix, AFG31022), is connected to the LDD to modulate the injection current to the TDL.

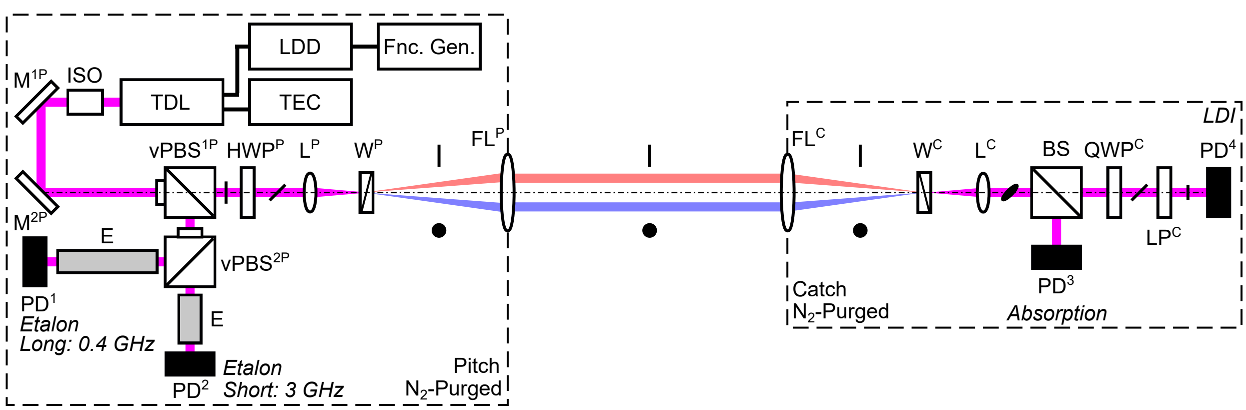

Fig. 1 Schematic of the A-LDI system. Components include a TDL, tunable diode laser; LDD, laser diode driver; TEC, temperature controller; ISO, optical isolator; M, mirror; vPBS, variable polarizing beamsplitter; E, etalon; PD, amplified photodiode; HWP, half-wave plate; L, lens; W, Wollaston prism; FL, field lens; BS, non-polarizing beamsplitter; QWP, quarter-wave plate; LP, linear polarizer. Superscripts *P* and *C* are used to denote *pitch* and *catch* sides of the system, respectively. Polarization states of light are roughly denoted by lines, circles, and ellipses.

The light output from the laser is linearly polarized and first transmits through a tunable optical isolator (ISO) designed for 760 nm light to reduce back-reflections into the laser which cause output instability. Two mirrors, M^{1P} and M^{2P} (Thorlabs, BB1-E03), fold the optical path and enable precise alignment of the beam on the main optical axis (dash-dot). A variable polarizing beamsplitter, $vPBS^{1P}$ (Thorlabs, VA5-780), is then used to adjust the transmission/reflection of the light. The reflected light passes through another identical $vPBS^{2P}$, which is again used to adjust the transmission/reflection of the light. The reflected light transmits through a solid YAG etalon with a free spectral range (FSR) of 0.4 GHz (LightMachinery) and is incident on an amplified photodiode with a gain setting of 0 dB, PD^1 (Thorlabs, PDA100A2). The transmitted light from $vPBS^{2P}$ passes through a second solid YAG etalon with an FSR of 3 GHz (0.1001 cm^{-1}), E (LightMachinery, OP-3091-27000), and is incident on a second amplified photodiode (gain setting of 0 dB), PD^2. The light that was initially transmitted through $vPBS^{1P}$ is linearly vertically polarized, and a half-wave plate, HWP^P (Thorlabs, WPHS05-780), rotates the linear polarization by 45° before entering a Wollaston prism with a 10 arcmin splitting angle, W^P (United Crystals). With this input polarization to the W^P, the coherent beam is split into two separate orthogonally polarized beams (red, blue) angled 10 arcmin relative to each other. A positive lens with a 40 mm focal length, L^P (Thorlabs, LBF254-040-B), is placed between the HWP^P and the W^P in order to focus the beam inside the W^P, and expand the two split beams out toward a field lens with a 75 mm focal length, FL^P (Thorlabs, LBF254-075-B). The W^P is placed at the focal point of L^P, and the FL^P is placed one focal length away from the W^P. This ensures that both beams travel parallel to each other, and that each beam is collimated as it traverses through the test gas of interest.

The two collimated, parallel beams (red, blue) transmit through the flow of interest, and another identical field lens on the opposite side, FL^C, focuses the beams down into a matching, albeit reversed, Wollaston prism, W^C. When positioned at the focal point of FL^C, the two beams are made colinear at the W^C, traveling again along the optical axis. A positive 40 mm focal length lens, L^C (Thorlabs, LBF254-040-B), collimates the colinear beams. A 70/30 reflection/transmission non-polarizing beamsplitter, BS (Thorlabs, BS023), mounted in a cage-cube mount (Thorlabs, CCM1-4ER), reflects 70% of the light into an amplified photodiode with a gain of 0 dB, PD^3, to measure the absorption signal. While both colinear beams are reflected at BS, they are not made to interfere, and so the absorption signal is insensitive to optical path length differences between the two beams. The remaining 30% of the light transmits through the BS, and because the phase of the two colinear beams may have become offset/delayed (and thus the effective polarization of the light is slightly elliptic), a quarter-wave plate, QWP^C (Thorlabs, WPQ05ME-780), is used to null out this ellipticity to return the light to nominal linear polarization. A linear polarizer, LP^C (Thorlabs, LPVISC050-MP2) makes the two colinear beams interfere, which are then incident on the fourth amplified photodiode at a gain setting of 10 dB, PD^4, to measure the LDI signal. The LP^C is rotated to the middle of the infinite interference fringe for maximum linear sensitivity and to avoid phase ambiguity. All photodiodes are connected to a four-channel Tektronix MSO 6 Series Oscilloscope with 50 Ω termination to digitize the signals.

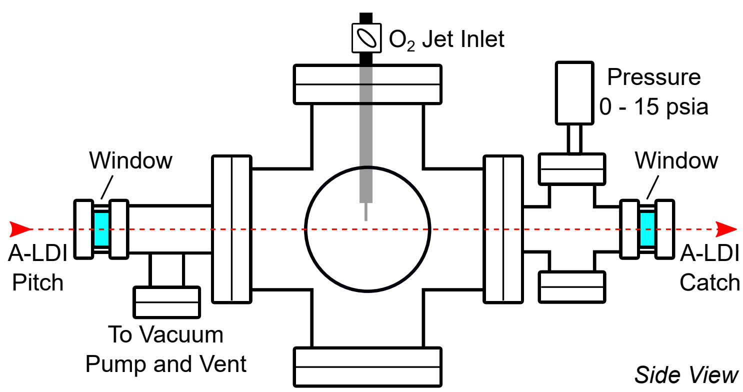

Fig. 2 Side-view schematic of the test cell with laser beam path shown in dashed red.

A sub-atmospheric pressure-controlled test cell, shown schematically from the side in Fig. 2, is used in the laboratory to evaluate the operation of the A-LDI system with 100% O_2 at pressures ranging from 1 atm down to ≈ 0.01 atm (14.7 psia to 0.15 psia). The two smaller windows (colored cyan in Fig. 2) were used to transmit the laser light through the test cell due to the long path length between these windows. The longer path length counters the relatively weak O_2 absorption in the A-band. These two windows were slightly wedged to avoid undesired optical etaloning effects. The test cell was placed on an optical table between the pitch and catch sides of the A-LDI instrument, such that the laser transmitted roughly through the centers of the test cell windows. In the center of the test cell, a hose with a nozzle at the end was inserted in a pass-through port to introduce a jet of 100% O_2 into the beam path as a density object for testing. The exit of the needle nozzle was placed just above the laser beam path to avoid obscuring the beam but also to provide a strong density gradient fluctuation near the beam. A ball valve was installed between the jet nozzle and the O_2 gas bottle regulator in order to keep the output pressure from the gas bottle constant for every test. The O_2 gas bottle regulator was set to its maximum output pressure, limited by a safety pop-off valve to 15 psia.

A vacuum pump was connected to a port on the pitch side of the test cell, with a ball valve to isolate the pump from the cell. An ambient laboratory gas venting valve was also located on this side of the test cell, again with a ball valve to isolate the laboratory atmosphere from the test cell when under vacuum. A pressure sensor for a 0-15 psia pressure range (Omega Engineering Inc., PX329-015A5V) was located in a pass-through port on the catch side of the test cell, far enough away from the vacuum port, the laboratory venting port, and the O_2 gas inlet port such that the pressure transients were dampened during testing (unlike the testing of Ref. [52]). The pressure sensor operates on a 5 V output scale with 0.25% static accuracy, and a linear fit to the discrete sensor calibration values gives the computed pressure as a function of measured voltage. The calibration equation for the pressure sensor (in psia) as a function of measured voltage, V, is given by: $P = 3.0069V - 0.061855$.

III. Laser and Acquisition System Operating Parameters

A. Laser Emission Wavelength Range

To enable precise laser wavelength set-points and scan ranges, the laser wavelength scanning windows as a function of TEC resistance/temperature were first identified. A simulation of the absorption spectrum for two pressures of 100% O_2 are plotted in Fig. 3 as a function of wavelength. The absorption feature peak wavelengths as defined in the HITRAN database are labeled with black text. Wavelength-scanned regions are indicated with colored boxes, with a scan range that generally encompasses three absorption features due to the laser injection current tuning limits. The colored boxes correspond to the colored text of the central absorption feature in the scan range, along with the associated TEC temperature setting used for each, reported both in the TEC-defined kΩ and the corresponding computed temperature in °C. A single anchor point is required to associate a temperature with an emission wavelength, which is provided in the laser datasheet as an emission wavelength of 760.8 nm for a temperature of 35°C (6.520 kΩ).

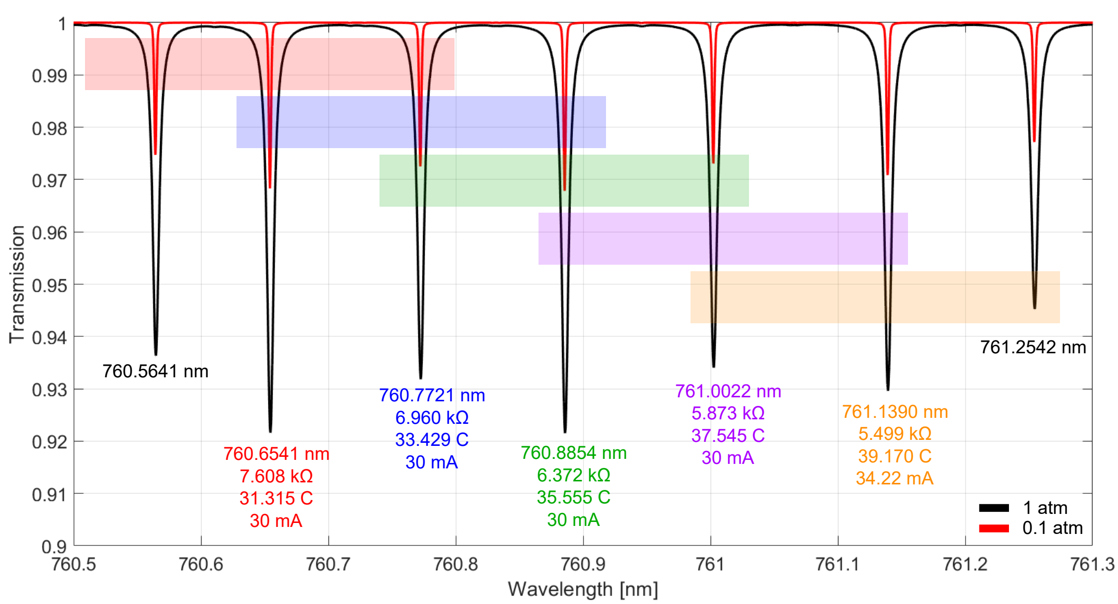

Fig. 3 Accessible absorption features of the tunable diode laser, with noted TEC temperature and LDD central injection current combinations. To access the full scan ranges highlighted in the colored rectangles, the laser injection current was tuned over its full range, from minimum (0 mA) to maximum (45 mA) allowable injection currents.

As the temperature was increased (resistance decreasing due to the negative temperature coefficient, NTC), the emission wavelength increased as the laser cavity grew in size, shifting the wavelength emission range window to the right in the plot. From the laser datasheet, the minimum and maximum operating temperatures are 30°C (8.046 kΩ) and 40°C (5.319 kΩ), respectively. From the figure, this laser can comfortably access seven absorption features ranging from 760.5 nm to 761.3 nm, although injection current tuning limitations only allows three absorption features to be accessed in a single laser scan at a time for a fixed temperature.

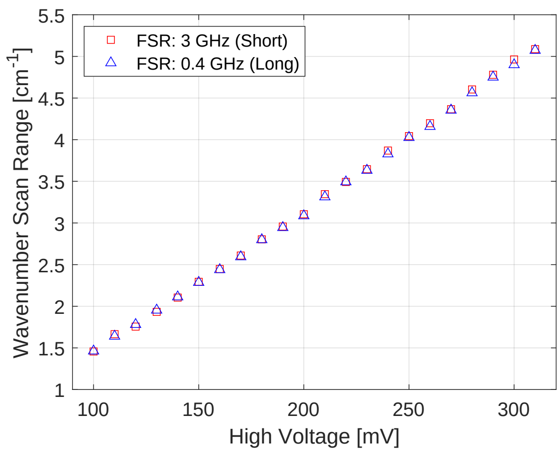

Fig. 4 Wavenumber scan range for increasing high voltage set-point values using data from both 3 GHz and 0.4 GHz etalons.

The low and high voltages of the function generator ramp input into the LDD can be chosen to scan over a desired wavelength range, as the input voltage range is converted to an injection current range. To determine how the scan range changes with an input voltage range, the low voltage was set to 0 mV and the high voltage set to an initial value of 100 mV. The fixed injection current value on the LDD was then set to a value so that the low voltage of 0 mV was just below the lasing threshold. This injection current value was approximately 11 mA, corresponding to the laser threshold current given in the manufacturer's datasheet. Keeping the low voltage and fixed LDD injection current the same, the high voltage on the function generator was increased from 100 mV to 310 mV in steps of 10 mV; going above the maximum voltage value of 310 mV caused the over-current protection on the LDD to trip. Using the etalon data as a wavenumber calibration, the maximum wavenumber scan range was plotted versus the high voltage set-point in Fig. 4. The results from both etalon data show the same trend, with linearly increasing wavenumber scan range as the high voltage set-point was increased. Note that the high voltage set-point could be reduced below 100 mV, but data were not taken at these lower values. However, due to the linear nature of this data, wavenumber scan ranges could be extrapolated down to lower high voltage set-point values. Because the high voltage of 310 mV was the largest value that could be used before the over-current protection was enabled on the LDD, these results show that the largest wavenumber scan range that could be attained was slightly greater than 5 cm^{-1}.

B. Slow-Scan and Modulation Frequencies

For WMS testing, the slow-scan frequency (f_s) and modulation frequency (f_m) combination for the laser diode driving waveform have an impact on the quality of the measured signals. In this section, the ranges of acceptable slow-scan frequencies and modulation frequencies are explored. Note that an upper limit on injection current tuning frequencies for the LDD used in this system is 150 kHz.

In the first test, the slow-scan frequency was kept fixed at $f_s = 50$ Hz, while the modulation frequency was changed to values of $f_m = 100$, 200, 300, 400, 500, 600, 700, 800, 900, 1000, 1250, 1500, 1750, and 2000 Hz, where the total frequency can be computed by multiplying f_s by f_m. The acquired data was processed using the WMS processing methodology outlined in Ref. [52], with a resulting plot of the second harmonic signal, normalized by the first harmonic signal, $S_{2f/1f}$, shown in Fig. 5a. The curves for modulation frequencies of 100 Hz and 200 Hz are not included, as these frequencies were too low for any usable signal. From the data plotted, all modulation frequencies appear to give reasonable WMS signals. A trend of increasing peak height with increasing modulation frequency is also seen, although the data of modulation frequency 300 Hz is no longer usable due to undesired oscillations. From these results, any modulation frequency at or above 400 Hz should be sufficient for good signal.

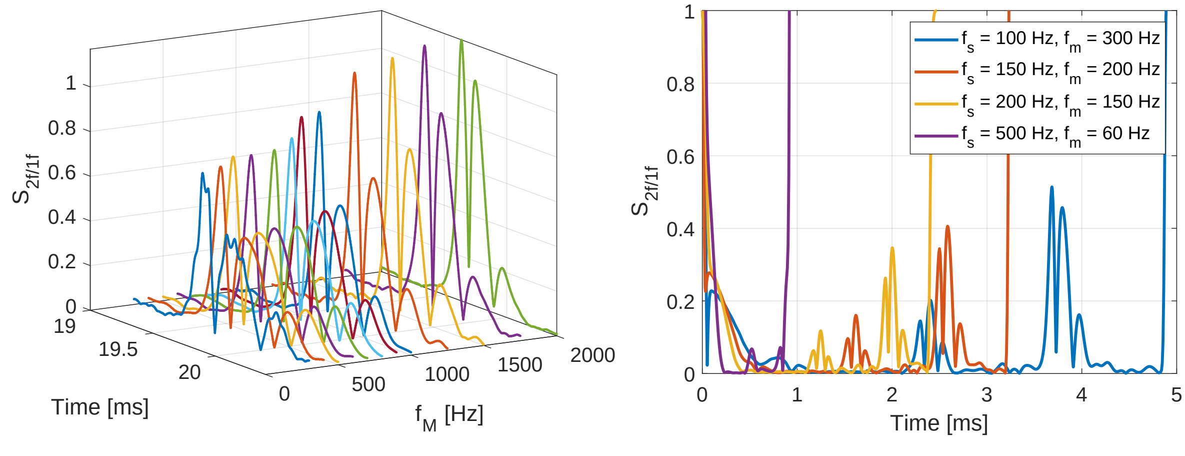

Fig. 5 $S_{2f/1f}$ **WMS signal for (a) varying modulation frequency** f_{m}**, and for (b) varying slow-scan frequency** f_{s} **with modulation frequency set to keep total frequency fixed at** $f_{\mathrm{t}} = 30$ **kHz.**

Next, the slow-scan frequency was changed to $f_{\mathrm{s}} = 100$, 150, 200, and 250 Hz, while f_{m} was changed such that the total modulation frequency remained at $f_{\mathrm{t}} = 30$ kHz ($f_{\mathrm{m}} = 300$, 200, 150, 60 Hz, respectively). A plot of the $S_{2f/1f}$ signal is plotted in Fig. 5b. The sharp increase in signal at the beginning and end of the datasets were from the start and end of the waveform, and roughly two absorption features are visible for each set. With a slow-scan frequency of 500 Hz, the absorption signal is low, and this setting is not recommended. With lower slow-scan frequencies and associated higher modulation frequencies, the $S_{2f/1f}$ signal appears acceptable. The lower the slow-scan frequency can be made, the faster the rate of the absorption measurements, since each absorption measurement is averaged over the period of each slow-scan ramp. From these results, any of the slow-scan frequencies below 200 Hz would be adequate.

C. Sampling Rate of Data Acquisition

A study was conducted to determine the minimum sampling rate that could be used for data acquisition of all signals relevant for the measurement (non-absorbing, etalon, absorbing, LDI). Using an excessive sampling rate will only make filtering of the resulting data in the digital lock-in amplifier (dLIA) take longer, and so finding a minimum required sampling rate is helpful to reduce data storage volume and computation time. Because the low-pass filtering uses a maximum value of 15 kHz (30 kHz/2), the limiting factor will end up being the etalon data set, with higher sampling rates needed for longer etalons with smaller FSRs.

In Fig. 6a, the raw absorption data are plotted (vertically offset for clarity) for all sampling rates tested, with no change to the experimental setup (test cell or laser operating characteristics) between data set acquisitions. The sampling rates are listed at the right side of the plot in units of MHz, with sampling rate increasing in the vertical direction. A wavelength-increasing (up-scan) and wavelength-decreasing (down-scan) of the slow-scan sinusoidal waveform is visible, with three absorption features present in each scan (at approximately 15 ms, 18 ms, and 22 ms for the up-scan). Most of the data sets look similar, but at the lower sampling rates, the waveforms begin to differ. The lowest four sampling rates (25 kS/s, 31.125 kS/s, 50 kS/s, and 62.5 kS/s) demonstrate what appear to be aliased signals, as would be expected since the modulation frequency of the laser is 30 kHz. The two sample rates close to this modulation frequency appear severely aliased (31.125 kS/s and 62.5 kS/s), while the other two are also aliased but less visibly so from this plot.

The differences in the data sets at the lower sampling rates can be more clearly seen when viewing the WMS second harmonic signal, R_2, of the 761.002 nm absorption feature (center feature in the scan, 18 ms). The plot in Fig. 6b shows select sampling rate R_2 data. All data sets greater than or equal to 312.5 kS/s are plotted in the same shade of grey, and are largely the same with only slight deviations in shape. Four selected lower sampling rates are plotted in color. The three lowest sampling rates demonstrate large deviations from the expected R_2 signal in grey, and at 250 kS/s, the shape

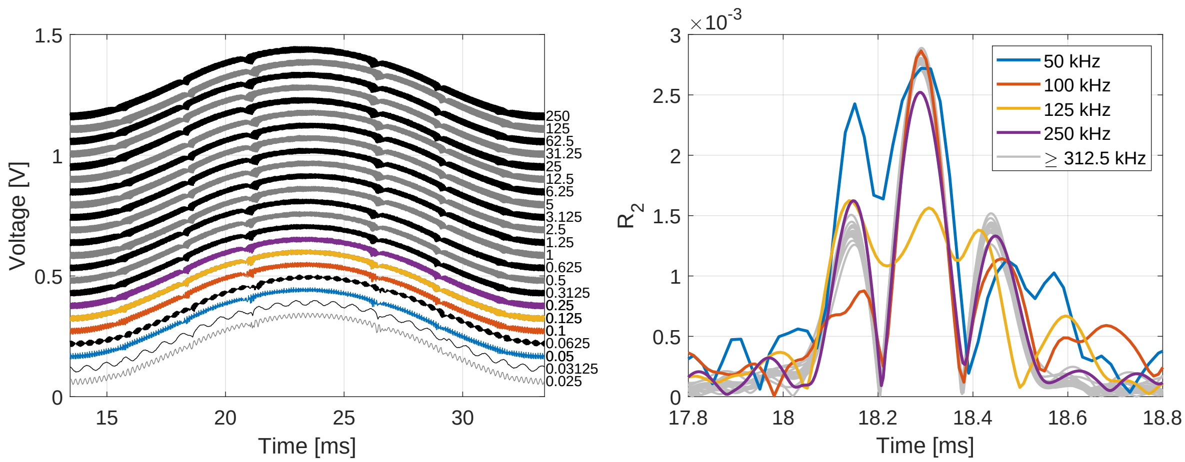

(a) **(b)**

Fig. 6 (a) Raw absorption signal up/down scan for all sampling rates tested, and (b) zoom view of second harmonic WMS data (R_2) for most sampling rates tested. Sampling rates for each data set are labeled at the right side of the plot, and colors in both plots correspond to each other.

is quite close to the expected shape, albeit with a reduced central peak value. These data demonstrate that the minimum sampling rate that should be used for these exact laser operation parameters is 312.5 kS/s.

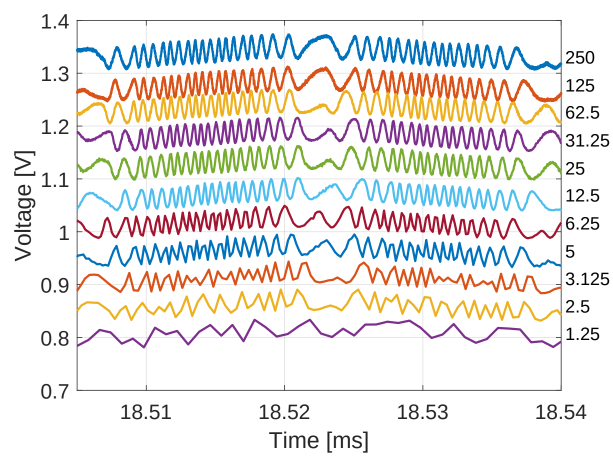

Fig. 7 Raw etalon signal for one cycle of modulation (up-scan/down-scan in wavelength) for a sub-set of sampling rates, listed at the right of the plot.

From the raw absorption data and WMS lineshapes, it was determined that the minimum sampling rate should be 312.5 kS/s. However, in these experiments it will be the etalon signal that dictates the minimum sampling rate, as evidenced by a zoom view of the etalon data shown in Fig. 7. Here, a single up-scan/down-scan of the laser during the fast modulation scan is shown with multiple peaks visible which are separated by the FSR of the etalon (0.4 GHz). To adequately convert the data from time to wavenumber/wavelength, these peaks must be resolved and identified precisely in time. As the sampling rate decreases from the maximum of 250 MS/s, the peaks remain resolved, but at 6.25 MS/s and below, the resolution of the data points that define the peaks becomes too low. Note that consideration must not only be given to the number of peaks identified in the trace of the etalon data, since the number of peaks may be adequate down to slightly lower sampling rates, but also the spacing of the peaks, since the precise spacing dictates where in wavelength-space the laser is currently emitting. If these peak spacing values are incorrect, then the fitting of the WMS etalon data will also be incorrect, and the simulations will not be able to accurately compute the best-fit gas properties from the measured data. This means that the etalon data dictates the lowest sampling rate for these measurements (since all channels on the oscilloscope must be acquired with the same sampling rate), and can be set to 12.5 MS/s. If a shorter etalon with a larger FSR is used, then the etalon minimum sampling rate can be reduced, although note that this will depend on the laser diode current driving frequencies that are being used. This lowest sampling rate of 12.5 MS/s is more than sufficient for the LDI measurements.

IV. Comparison of 3 GHz and 0.4 GHz Etalons

When aiming to make measurements at the lower pressures characteristic of high speed wind tunnels, the modulation depth (a_m) of the modulation frequency (f_m) of the WMS waveform may be quite small, since its optimum value is proportional to the width of the absorption feature. For narrower absorption features such as those expected at lower pressures, this modulation depth becomes exceedingly small. The etalon used in Ref. [52], a 3 GHz solid YAG etalon approximately 27 mm long, provided a sufficient number of fringe peaks for fitting both DAS data and higher modulation depth WMS data. It was noted in that paper, however, that should lower pressure quantitative results be desired, a longer etalon with a smaller free-spectral range would be required. Comparisons of a new 0.4 GHz etalon with the original 3 GHz etalons are made here.

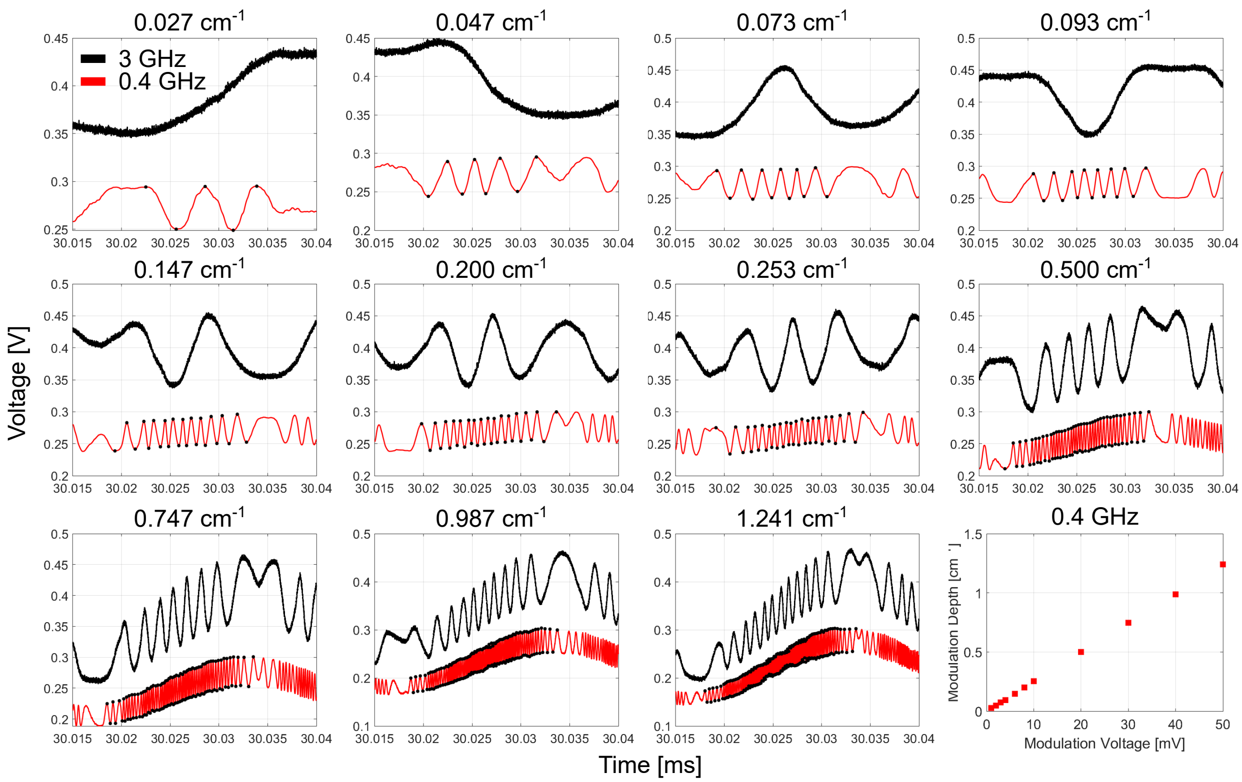

Fig. 8 Raw etalon data for a 3 GHz etalon (black) and 0.4 GHz etalon (red), with black circular markers denoting peaks and troughs of 0.4 GHz etalon signal. Modulation depth versus modulation voltage amplitude is plotted at the bottom-right for the 0.4 GHz etalon.

The signals from the light transmitting through both etalons were simultaneously sampled, the 0.4 GHz signal on PD^1 and the 3 GHz on PD^2, as per the schematic in Fig. 1. The optical path was purged with N_2 gas to eliminate any absorption due to O_2. A linear ramp waveform was used to modulate the injection current of the laser, where the peak-to-peak voltage of the ramp was 250 mV, the slow-scan frequency was f_s = 50 Hz, and the modulation frequency was f_m = 600 Hz (total frequency $f_t = f_s f_m$ = 30 kHz). Varying modulation voltage amplitudes were used ranging from 1 mV to 50 mV.

Plots of the raw voltage versus ramp time for all modulation voltage amplitudes and the 3 GHz (black) and 0.4 GHz (red) etalons are shown in Fig. 8 (except for the lower-right subplot), where the time bounds are chosen to only display one half of a modulation (increasing wavelength scan). In each subplot, the peaks of the 0.4 GHz data are identified with black markers. Using these identified etalon fringe peaks and troughs, the known FSR of the etalon was used to compute the modulation depth of the scan. Note that each adjacent marker increments the wavenumber by one half of an FSR because both peak and trough data are used. These computed modulation depth values are noted above each respective plot, and are plotted in the bottom-right subplot of Fig. 8. The modulation depth increases linearly with the modulation voltage amplitude. The largest modulation depth of approximately 1.25 cm^{-1} is approximately 30% of the amplitude of the entire scan range of the slow-scan ramp, using the data from Fig. 4, where a peak-to-peak voltage of 250 mV corresponds to a scan range of approximately 4 cm^{-1}. At the higher modulation depths, the 3 GHz etalon signal has a sufficient number of peaks to compute an accurate time-to-wavenumber calibration (t-ν). As the modulation depth decreases (to optimize WMS absorption signals at lower pressures, for example), the number of peaks in the 3 GHz data decreases to a point where an accurate calibration cannot be reliably computed; the data for a modulation depth of 0.253 cm^{-1} is likely the last data that can be used. However, the data from the 0.4 GHz etalon at even the lowest modulation depth still provide a sufficient number of peaks to fit a calibration curve.

V. Effect of Etalon Beam Incidence Angle

The FSR of the etalon is specified by the material's index of refraction and the path length of the light through the material. The desired operation of the etalon is with orthogonal incident light on its entrance face (0°), providing optimum interference of the reflected and transmitted beams. However, the etalon may be angled slightly relative to the beam propagation axis and still retain an etalon signal with high enough finesse to determine the t-ν calibration. When the incident beam angle relative to the etalon's axis is increased from 0°, the FSR changes slightly, the peak-to-peak amplitude of the etalon fringe signal decreases due to misalignment of the transmitted beams, and the fringes shift in wavelength. This section evaluates how much, if any, impact the angling of the etalon axis with respect to the laser beam has on the t-ν calibration.

The peak-to-peak voltage of the linear ramp used to modulate the injection current was 200 mV, resulting in a wavenumber scan range of approximately 3 cm^{-1} using the data of Fig. 4. Three data sets were acquired for both the 3 GHz and 0.4 GHz etalons, with raw data plotted for a single ramp in Figs. 9a and 9b, respectively. The etalons were first angled such that the peak-to-peak signal of etalon fringes was maximized, and this was assumed to be the beam-normal incidence angle (plotted in black). Next, the etalons were angled to an off-normal incidence angle until the peak-to-peak fringe signal decreased to some lower value (plotted in red). Finally, the etalons were angled such that no discernible fringe signal was visible (plotted in blue). A simplified schematic representation of two transmitted beams is shown in Fig. 9, where each beam is denoted by a solid colored circle, and the region of overlap (i.e., interference) is denoted by the appropriate transparent color. The black schematic shows perfect overlap of the beams, with interference over the entire beam diameter and a large peak-to-peak fringe amplitude. The red schematic shows the two beams slightly offset from one another, but still with a region of overlap/interference, causing a reduction in the peak-to-peak amplitude of the etalon fringes from the orthogonal case. The blue schematic shows the two beams entirely separate from one another, with no region of overlap/interference, and so no etalon fringes are visible.

The raw data from Fig. 9 were smoothed and the peaks of the oscillating waveform were identified. For each identified peak, the wavenumber was incremented by the FSR of the appropriate etalon, and the relative wavenumber was plotted versus time in Fig. 10, where the data were all shifted such that the first peak occurred at a time of 0 ms. This shifting was required to align the two relative wavenumber data sets since, as can be seen in the insets of Fig. 9, the fringe peaks in the black and red data are shifted in time relative to one another, another consequence of the angling of the beams, discussed in more detail later. The orthogonal (black) and angled (red) plots are well-aligned, and show that at these beam angles, the t-ν transformation is not changed sufficiently to be noticed.

The equation for the FSR of the solid YAG etalon is given by Eq. (1), where c is the speed of light in a vacuum, n is the index of refraction of the material (here, $n = 1.8171$), L is the length of the etalon, and θ is the incidence angle of the light (0° being orthogonal to the entrance face of the etalon).

$$\mathrm{FSR} = \frac{c}{2nL\cos(\theta)} \tag{1}$$

As the laser incidence angle increases from its optimal orthogonal entrance at the etalon, the FSR increases. The result of this is that the angled-beam t-ν calibration will show an artificially increased scan range. This so-called tilt-tuning is

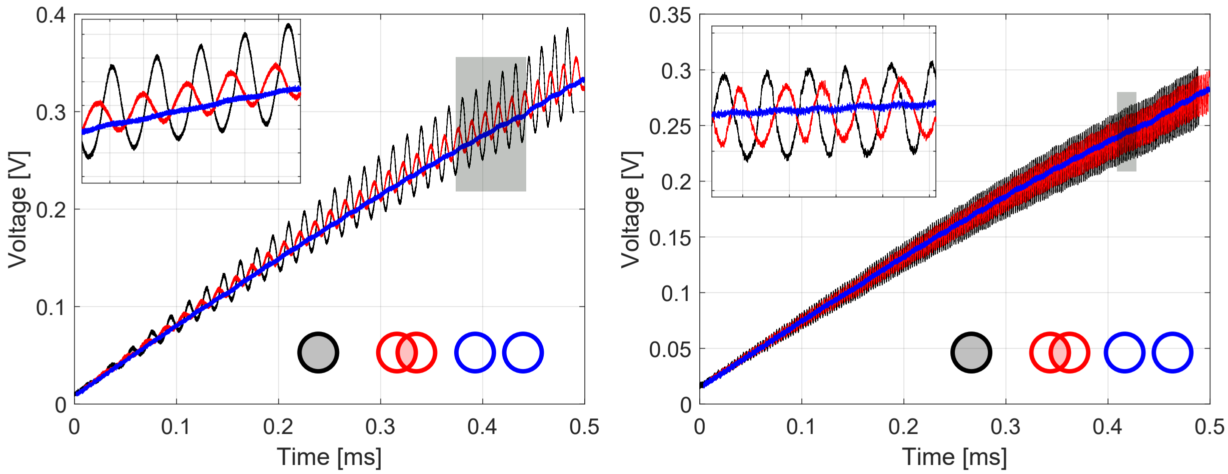

(a) (b)

Fig. 9 Three beam incidence angle raw etalon data sets (black, red, blue) for (a) the 3 GHz **etalon and (b) the** 0.4 GHz **etalon, with schematic depictions of two transmitted beams at the bottom right of each plot, and zoom-view regions highlighted in gray.**

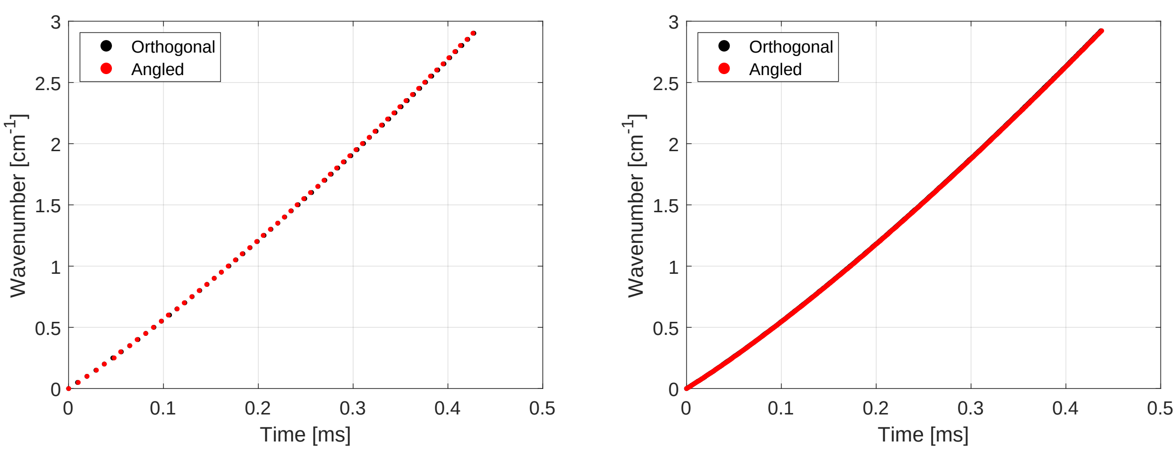

(a) (b)

Fig. 10 Relative wavenumber versus time calibration plots for (a) the 3 GHz etalon and (b) the 0.4 GHz etalon, with colors corresponding to the raw data of Fig. 9.

typically deliberately used to adjust the transmission wavelength of the etalon, and an application for this adjustment will be discussed in Section VI.

As the laser beam incidence angle is increased, the transmission peaks move to shorter wavelengths (i.e., longer wavenumbers). The wavelength shift effect with increasing incidence angle is shown plotted in Fig. 11a, for five angles including normal incidence at 0°. These data were computed using LightMachinery's etalon designer tool, showing a shift of approximately 0.001 nm over 4° of tilt angle, although note that the shift is nonlinear. This shifting can also be seen in the raw data of Fig. 11b, where each data set has been truncated to just one fringe for clarity. The right-most blue data set was taken at 0° incidence angle, and as the etalon was tilted further, the fringe peak shifted lower in time (corresponding to a lower wavelength), and the peak fringe amplitude decreased. Note that the etalon angling steps used for the data in Fig. 11b were not linear, and so information about the peak shift as a function of angle cannot be computed here.

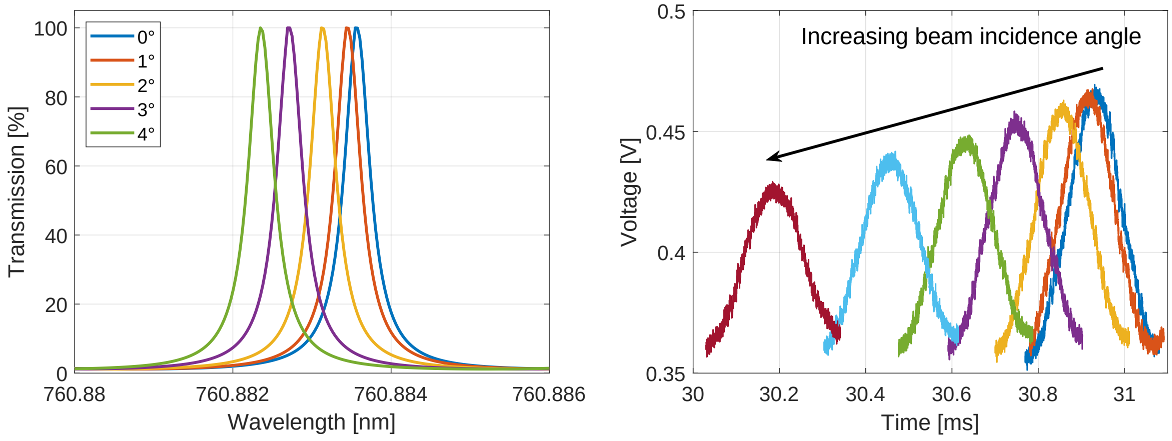

(a) **(b)**

Fig. 11 (a) Simulations of etalon fringe peak shift to lower wavelength as a function of incident beam angle, and (b) experimental data of etalon fringe position with a change in incident beam angle.

VI. Fixed-Wavelength DAS

Absorption systems are typically used in a scanned-wavelength mode, which allows detailed measurements of the absorption lineshapes, and thus higher quality determination of the flow properties. In Ref. [52], it was shown that the A-LDI system could also be operated in a constant-current mode, where the laser wavelength is fixed, either outside any absorption features (akin to a conventional LDI/FLDI system, and called *off-peak*), or near the center of an absorption feature (called *on-peak*). In Fig. 12, off-peak (black) and on-peak (gray) measurements are shown in the plot to the right. The positioning of the laser voltage in the ramp is schematically shown at the left, where the black data are located between two absorption features, and the gray data are located near the center of an absorption feature. With increasing time, the O_2 concentration in the test cell increases causing the measured voltage of the on-peak data to decrease as expected. The black data, however, remains constant because the emission wavelength is not absorbed by O_2.

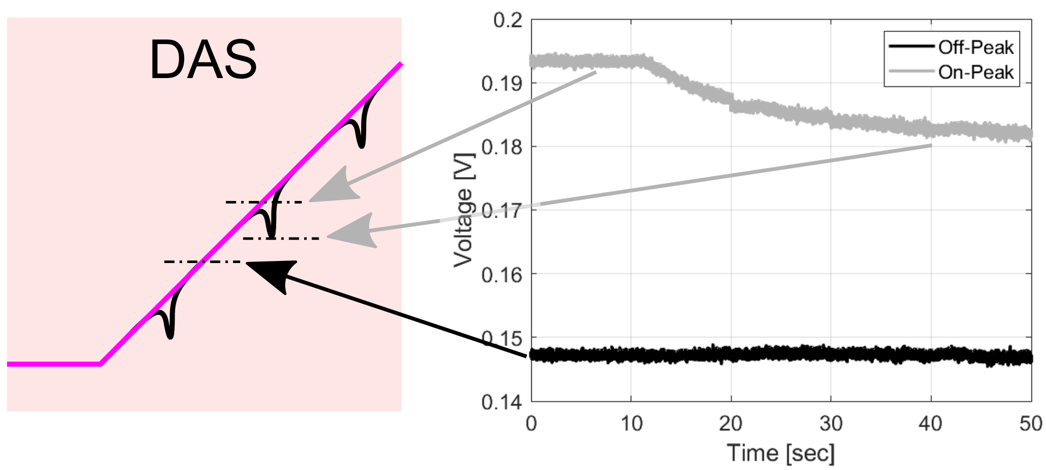

Fig. 12 Constant current/wavelength on-peak (gray) and off-peak (black) absorption measurement with increasing O_2 in the test cell over time. Approximate representations of the voltages in the plot are shown in the schematic at the left.

It was determined that the measurements were sensitive to absorption changes in the flow, but that precise knowledge of the laser's wavelength would be required to determine accurate flow properties from simulations. While the use of high-resolution wavemeters is currently being investigated, their cost and resolution may be prohibitive. This section explores a low-cost alternative using the available etalons which have been used for scanned-wavelength DAS and WMS measurements.

A. Etalon as a Relative Wavemeter: Concept Description

It was thought that the etalons that had been used as a t-ν calibration in scanned-wavelength DAS and WMS measurements could also be used as a low-cost relative wavemeter alternative for these constant-wavelength measurements. As light passes through the etalon, constructive and destructive interference occurs between the reflected and transmitted beams, and is measured as a change in intensity by the photodiode. As the laser wavelength is scanned, the signal increases and decreases due to the changing constructive and destructive interference, with two of these constructive peaks shown in the schematic plot of Fig. 13. Here, the measured intensity from the photodiode is plotted against the wavelength. The laser wavelength can be changed by either changing the injection current (via the LDD) or the temperature (via the TEC). The two fringe peaks are separated by the FSR of the etalon. For constant-current fixed-wavelength measurements, the laser wavelength is no longer scanned, and instead of the sinusoidal-type plot seen in Fig. 13, a single intensity value will be measured at the photodiode. The value of this fixed intensity from the light passing through the etalon will depend on the wavelength of the laser, and is shown in the figure with five colored circles depending on their wavelength. The gray circle corresponds to the shortest wavelength while the magenta corresponds to the longest wavelength.

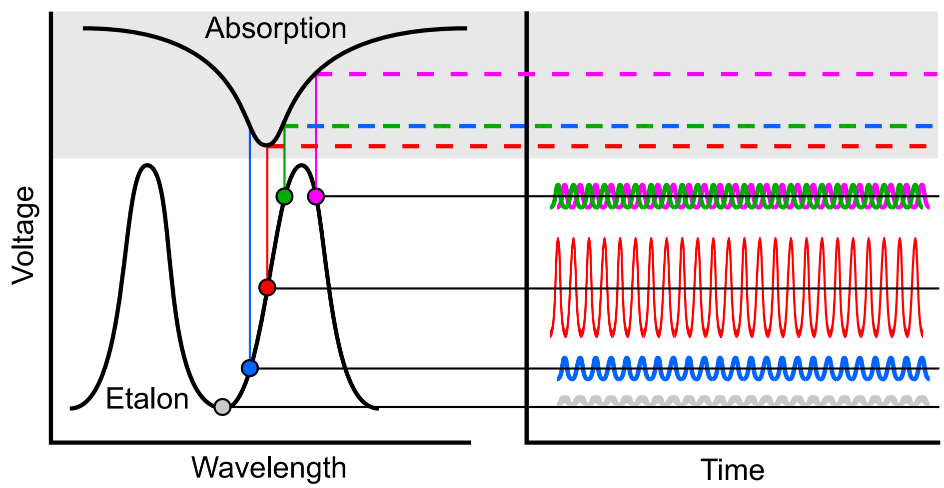

Fig. 13 Schematic of the fixed-wavelength relative wavemeter concept, using the etalon fringe as a monitor of relative wavelength change.

Above the etalon signal in the figure, a characteristic absorption feature is shown. The absorption feature is located relative to the etalon peak such that at the linecenter, the corresponding etalon fringe voltage is approximately halfway between the trough and the peak, denoted by the red circle. At a slightly shorter wavelength, the corresponding etalon fringe voltage has shifted lower towards the trough (blue circle), whereas for a slightly longer wavelength, the corresponding etalon fringe voltage has shifted higher towards the peak (green circle). Consider a $\Delta\lambda$ wavelength oscillation about the wavelength set-point. For the red set-point, this $\Delta\lambda$ oscillation will result in a large oscillation of the etalon fringe voltage as a function of time, seen in the right plot of the schematic in red. For the blue and green set-points, the same $\Delta\lambda$ wavelength oscillation results in a smaller amplitude etalon fringe voltage oscillation, again shown in the time series data schematic at the right. Note that the directionality of the wavelength change is known, where an increase in the wavelength corresponds to an increase in the measured fringe voltage, and a decrease in the wavelength corresponds to a decrease in the measured fringe voltage. If the linecenter of the absorption feature were located on the other side of the fringe, this correspondence would be inverted, but still known. The slope of the etalon fringe at the wavelength set-point determines the sensitivity of the fringe voltage change to a change in wavelength, $\Delta V_{\text{etalon}}/\Delta\lambda$.

At the wavelength set-point corresponding to the trough of the etalon fringe signal (gray circle), the $\Delta\lambda$ oscillation still results in an oscillation of the etalon fringe voltage in time, but with reduced magnitude, and with an ambiguity about whether the wavelength is increasing or decreasing, because both cause an increase in the etalon fringe voltage signal. It is best to avoid a measurement wavelength that places the signal at either the trough or the peak of the etalon fringe due to these ambiguities. Another ambiguity in the etalon signal is demonstrated with the green and magenta circles in Fig. 13, which, with the $\Delta\lambda$ oscillation, result in the same etalon fringe voltage signal. In this scenario, it is unclear from the etalon data whether the wavelength corresponded to the green or magenta wavelength. Thus, it is best to keep any shifting of the wavelength on one side of the etalon fringe, between the trough and the peak. The dashed lines showing the absorption signal voltage show an ambiguity between the green and blue data, where both these wavelength set-points would result in the same absorption signal being measured. This is not a problem, however, because the blue and green etalon fringe voltages are separated (lower fringe voltage corresponds to a lower wavelength, and vice versa).

Using the scenarios outlined in Fig. 13, some general etalon selection guidelines can be discussed. Since there should be no etalon peak ambiguity with a change in wavelength, the linecenter of the absorption feature should be placed near the half-amplitude of the etalon fringe. The increase/decrease in wavelength of the laser will be apparent given an associated increase/decrease or decrease/increase in etalon voltage signal, depending on which side of the fringe was chosen. The expected shift of the laser during testing should be fully encompassed by one side of the etalon fringe, and so a rule-of-thumb for the etalon design is that half the FSR is equal to the full-width at half-maximum (FWHM) of the absorption feature. For the highest sensitivity to a shift in wavelength, the slope should be high, although note that laser noise (among other factors) also contributes to a noisy etalon output voltage. For a larger fringe slope at the half-amplitude position, the finesse of the etalon should be high. However, it might be useful to have a smaller slope for smaller changes in the etalon voltage with associated wavelength, and so a lower finesse may also be acceptable. This can be accomplished by, for example, reducing the mirror reflectivity, which may also reduce the cost. There are design trade-offs between finesse/slope, FSR, and cost.

B. Etalon as a Relative Wavemeter: Measurements

To be able to use the etalon as a relative wavemeter, it must be determined where exactly in wavelength space the absorption peak is located relative to the etalon signal output. A typical scanned-wavelength DAS ramp can be acquired prior to the fixed-wavelength measurements to determine the relative positions of the etalon fringe and the absorption feature of interest. A plot of the absorption feature of interest is shown in Fig. 14a in black (right axis). The time bounds for this plot are narrow because the region near the absorption feature linecenter is of interest. Various etalon fringe signals are plotted on the left axis in colored data, where the right-most blue data show the 0° incidence angle etalon orientation. A dashed black line at the absorption feature linecenter shows that this normal incidence etalon angle places the linecenter close to the peak of the etalon fringe, which is not ideal for wavelength shift sensitivity. As the beam incidence angle was increased, the etalon fringes shifted to lower times (lower wavelengths). From the design guidelines of Section VI.A, the etalon was angled to place the absorption linecenter at the middle of the fringe, corresponding roughly to the yellow etalon data in Fig. 14a.

A plot of the etalon fringe voltage for the final selected etalon angle is shown in Fig. 14b, where the data from the 3 GHz etalon are shown in green (left axis), and the absorption signal is shown in black (right axis). The absorption linecenter was not located exactly at the fringe half-peak value, but there is still usable sensitivity to wavelength changes. Note that the etalon fringe voltages in Fig. 14a are smoothed for clarity, but the raw data are shown in Fig. 14b. From this etalon fringe position relative to the absorption feature linecenter, a decrease in wavelength will result in an increase in etalon fringe voltage, while an increase in wavelength will result in a decrease in etalon fringe voltage. Due to the slight offset from the fringe-half peak value, a decrease in wavelength will result in a higher sensitivity etalon voltage change than an increase in wavelength.

To test the fixed-wavelength absorption measurement concept, the sub-atmospheric pressure-controlled test cell outlined in Section II was used. The pitch and catch sides of the A-LDI system were purged with N_2 gas to eliminate absorption of the laser due to O_2. The test cell was first evacuated to approximately 0.01 atm using a vacuum pump. Acquisition of the etalon and absorption signals was triggered, and the O_2 gas inlet port was opened, with the test cell continuously filling with 100% O_2 over a duration of 50 seconds, until the test cell pressure reached nearly 1 atm. Because a single acquisition record length was limited to 10 seconds, five separate records were acquired and stitched together. For the first of the five acquisitions, the O_2 port remained closed, and this data set was used as a baseline transmission value, using the assumption that the entire path length was evacuated of any absorption gases.

Three tests were conducted, the first with the injection current set such that the wavelength of the laser was as close

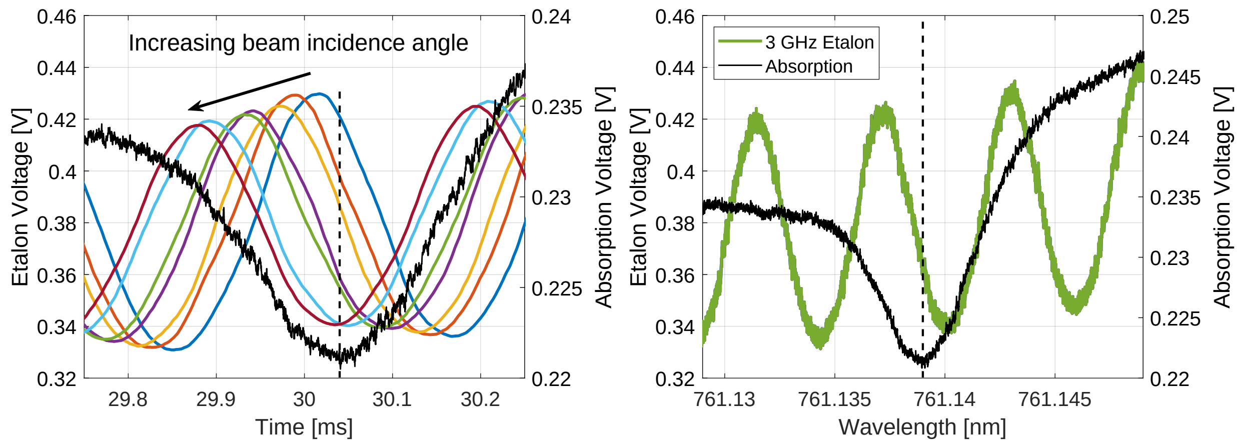

(a) **(b)**

Fig. 14 Plots of voltage versus (a) time and (b) wavelength for the etalon fringe data and absorption data. Multiple etalon beam incidence angle data sets are plotted in (a), and final selected etalon angling shown in (b).

as possible to the absorption linecenter, within the resolution of the LDD (0.01 mA). Next the injection current was decreased by ≈ 0.1 mA from its linecenter value, and the pump-up testing was conducted again. Finally, the injection current was increased by ≈ 0.1 mA from its linecenter value, and the pump-up testing was conducted a final time. A plot of probed absorption feature is shown in Fig. 15a, where the vertical dashed red line denotes the location of the linecenter, ν_0. The fixed-wavelength results from the test with the laser wavelength at the absorption feature linecenter are shown in Fig. 15b, where the off-peak data are shown in black and the on-peak absorption data are shown in gray, where every 1000th data point is plotted. The pressure was continuously monitored in the test cell during the entire acquisition, and using this pressure data, HITRAN simulations of the absorption feature for each data point can be computed. For the results presented in this paper, only 20 data points throughout the 50 second test duration are simulated to save time. After the absorption feature has been simulated for the known pressure, path length, gas concentration, and temperature, the transmission value (e.g., from Fig. 15a) at the known wavelength is extracted, and plotted with red circles in Fig. 15b. These simulated results of the expected transmission closely match those of the measured transmission.

Data from the shorter wavelength testing are plotted in Fig. 15c, where the linecenter transmission values are again plotted with red circles for comparison. The gray measured transmission data are now different than the linecenter data, and exhibit less absorption as expected away from the linecenter. The pressure values at each time were used to compute the HITRAN simulations of the absorption feature, as was done for the linecenter case. Now, instead of extracting the linecenter transmission value, the transmission value must be extracted at the correct wavelength. The etalon data, continuously monitored during the pump-up testing, were used in conjunction with the dataset of Fig. 14b to determine the wavelength shift. The change in measured etalon voltage was converted to a change in the wavelength from the known linecenter wavelength, and this wavelength was used to extract the transmission, which is plotted with blue circles in Fig. 15c. Because the etalon voltage drifts slightly over the duration of the 50 second test, the wavelength also shifts slightly, and this is accounted for at every plotted data point. The wavelength drift is visualized in the plot of Fig. 15a, although this drift is minimal. In contrast, the fixed-wavelength absorption data of the longer wavelength testing can be seen to have a large etalon voltage shift (purple region in Fig. 15a), corresponding to quite a large wavelength drift over the run duration. However, even with a large wavelength drift, with the etalon voltage continuously monitored and the wavelength used for the transmission extraction adjusted, the simulations agree well with the measured absorption data, as shown with the purple circles in Fig. 15d. These measurements demonstrate that it is possible to use a low-cost etalon as a relative wavemeter for fixed-wavelength absorption measurements. The benefit of using the fixed-wavelength method of obtaining the absorption measurement is that instead of the retrieved density being an average over the period of the slow-scan ramp, it results in a density measurement at the same sampling rate as the interferometry system.

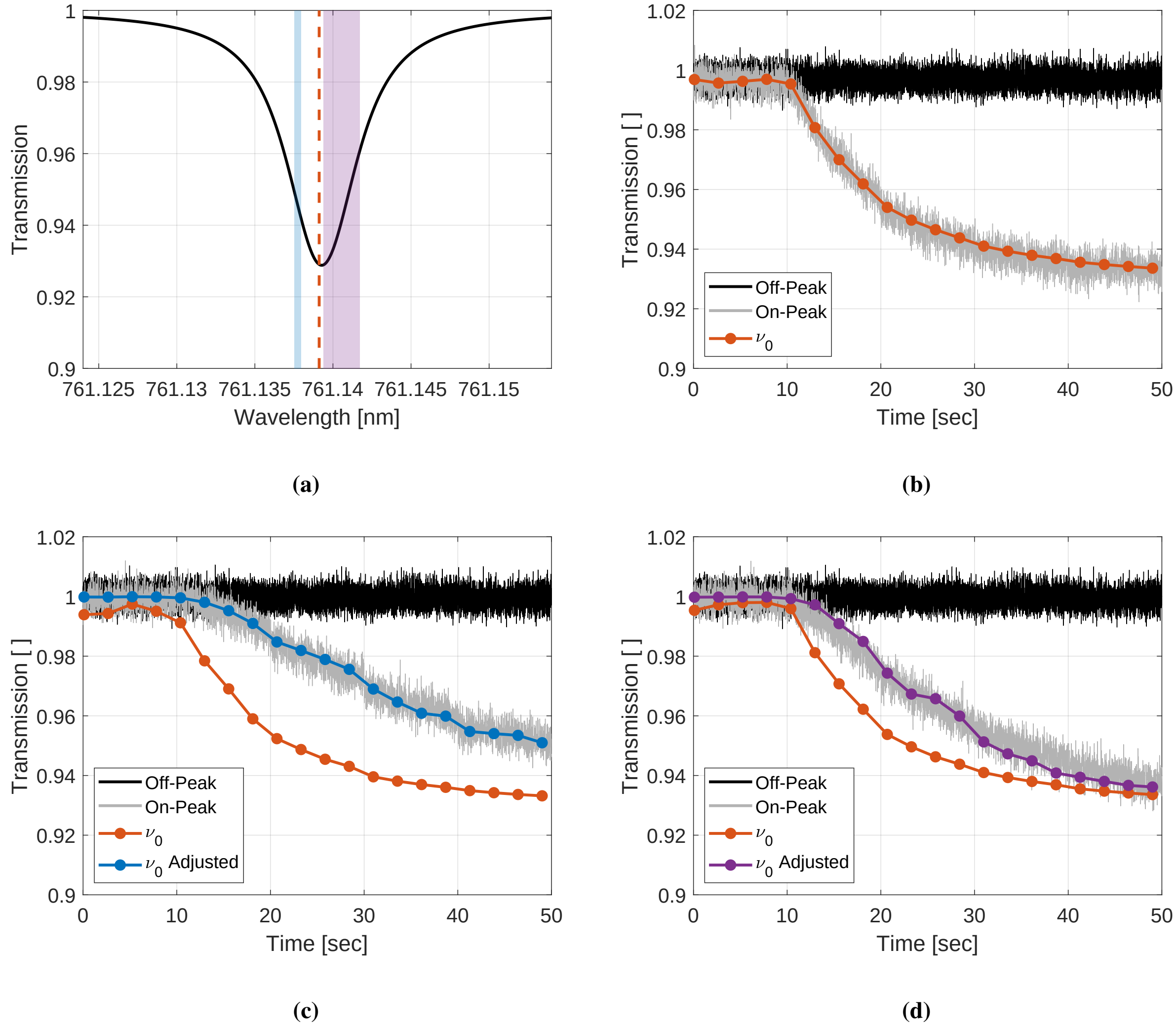

Fig. 15 (a) Transmission versus wavelength of probed absorption feature, with colored regions corresponding to the wavelength range of the measurements in (b-d). (b-d) Comparison of measured fixed-wavelength data (gray) and simulated transmission data (colored circles) for three wavelength positions: (b) at the absorption feature linecenter, (c) shifted to lower wavelengths, and (d) shifted to higher wavelengths.

VII. Conclusions

Further characterization progress of an absorption laser differential interferometer was made, in order to help the development of high-speed simultaneous, colinear measurements of flow properties (pressure, temperature, concentration, velocity) and flow fluctuations. Characterization of the laser operating parameters was first performed, allowing for precise setting of the laser wavelength for fixed-wavelength measurements using the laser injection current and temperature. Looking forward to further WMS testing of the system, the optimum slow-scan and modulation ramp frequencies were identified, and the minimum sampling rate that can be used for the measurements was prescribed. A slow-scan frequency lower than 200 Hz can be used, with the modulation frequency value chosen such that the total modulation frequency is 30 kHz. For lower-pressure WMS measurements, a smaller modulation depth will be required for good WMS signal. A new, longer etalon 0.4 GHz was compared with a shorter 3 GHz etalon used in previous testing. The minimum modulation depth that the 3 GHz can likely resolve for a good time-to-wavenumber calibration is approximately 0.253 cm^{-1}. The effect of angling the laser beam incidence angle when transmitting through the etalons was investigated. It was determined that there was no appreciable change in the FSR of the etalon when angled even to extreme angles. Angling the etalon can be used to shift the etalon fringe location in wavelength space. This shifting of the etalon fringe signal enables the use of the etalon as a low-cost relative wavemeter for fixed-wavelength measurements. These fixed-wavelength measurements are desired such that the absorption and LDI measurements are simultaneously sampled at the same sampling rate, enabling a truly simultaneous measurement of both mean gas density and density fluctuations. Testing with a test cell at pressure ranging from 0.01 atm to atmospheric pressure validated the use of the etalon as a relative wavemeter, and comparisons of measured and simulated data are promising, but require further exploration.

Acknowledgments

This work was supported by the NASA Transformation Tools and Technologies (TTT) project and the Hypersonic Technologies Project (HTP). Specific vendor and manufacturer names are explicitly mentioned only to accurately describe the test hardware. The use of vendor and manufacturer names does not imply an endorsement by the U.S. Government nor does it imply that the specified equipment is the best available.

References

[1] Gladstone, J. H., and Dale, T. P., "Researches on the Refraction, Dispersion, and Sensitiveness of Liquids," *Philosophical Transactions of the Royal Society of London*, Vol. 153, 1863, pp. 317–343. URL `http://www.jstor.org/stable/108799`.

[2] Smeets, G., "Laser-Interferometer Zur Messung An Schnellveränderlichen Schwachen Phasenobjekten," *Optics Communications*, Vol. 2, No. 1, 1970, pp. 29–32. doi:10.1016/0030-4018(70)90023-4.

[3] Smeets, G., "Laser Interferometer for High Sensitivity Measurements on Transient Phase Objects," *IEEE Transactions on Aerospace and Electronic Systems*, Vol. AES-8, No. 2, 1972, pp. 186–190. doi:10.1109/taes.1972.309488.

[4] Smeets, G., and George, A., "Laser-Differential Interferometer Applications in Gas Dynamics," Tech. Rep. 28/73, Institut Franco-Allemand de Recherches Saint-Louis, Nov. 1973.

[5] Parziale, N. J., Shepherd, J. E., and Hornung, H. G., "Free-stream density perturbations in a reflected-shock tunnel," *Experiments in Fluids*, Vol. 55, No. 1665, 2014. doi:10.1007/s00348-014-1665-0.

[6] Danehy, P. M., Weisberger, J., Johansen, C., Reese, D., Fahringer, T., Parziale, N. J., Dedic, C., Estevadeordal, J., and Cruden, B. A., "Non-Intrusive Measurement Techniques for Flow Characterization of Hypersonic Wind Tunnels," Tech. rep., Flow Characterization and Modeling of Hypersonic Wind Tunnels (STO-AVT-325), Von Karman Institute, Brussels Belgium, Dec. 2018.

[7] Birch, B., Buttsworth, D., and Zander, F., "Measurements of freestream density fluctuations in a hypersonic wind tunnel," *Experiments in Fluids*, Vol. 61, No. 7, 2020. doi:10.1007/s00348-020-02992-w.

[8] Gillespie, G. I., Ceruzzi, A. P., and Laurence, S. J., "A multi-point focused laser differential interferometer for characterizing freestream disturbances in hypersonic wind tunnels," *Experiments in Fluids*, Vol. 63, No. 11, 2022. doi:10.1007/s00348-022-03522-6.

[9] Lawson, J. M., Neet, M. C., Hofferth, J. W., and Austin, J. M., "Supersonic Freestream Density Fluctuations from Focused Laser Differential Interferometry and Pitot-Probe Measurements," *AIAA Journal*, Vol. 60, No. 9, 2022, pp. 5173–5186. doi:10.2514/1.j061432.

[10] Parziale, N. J., Shepherd, J. E., and Hornung, H. G., "Differential Interferometric Measurement of Instability in a Hypervelocity Boundary Layer," *AIAA Journal*, Vol. 51, No. 3, 2013, pp. 750–753. doi:10.2514/1.j052013.

[11] Parziale, N. J., Shepherd, J. E., and Hornung, H. G., "Observations of hypervelocity boundary-layer instability," *Journal of Fluid Mechanics*, Vol. 781, 2015, pp. 87–112. doi:10.1017/jfm.2015.489.

[12] Jewell, J. S., Parziale, N. J., Leyva, I. A., and Shepherd, J. E., "Effects of Shock-Tube Cleanliness on Hypersonic Boundary Layer Transition at High Enthalpy," *AIAA Journal*, Vol. 55, No. 1, 2017, pp. 332–338. doi:10.2514/1.j054897.

[13] Bathel, B. F., Weisberger, J. M., Herring, G. C., King, R. A., Jones, S. B., Kennedy, R. E., and Laurence, S. J., "Two-point, parallel-beam focused laser differential interferometry with a Nomarski prism," *Applied Optics*, Vol. 59, No. 2, 2020, pp. 244–252. doi:10.1364/ao.59.000244.

[14] Weisberger, J., Bathel, B., Herring, G., Buck, G., Jones, S., and Cavone, A., "Multi-point line focused laser differential interferometer for high-speed flow fluctuation measurements," *Applied Optics*, Vol. 59, No. 34, 2020. doi:10.1364/ao.411006.

[15] Gragston, M., Siddiqui, F., and Schmisseur, J. D., "Detection of second-mode instabilities on a flared cone in Mach 6 quiet flow with linear array focused laser differential interferometry," *Experiments in Fluids*, Vol. 62, No. 4, 2021. doi:10.1007/s00348-021-03188-6.

[16] Hopkins, K. J., Porat, H., McIntyre, T. J., Wheatley, V., and Veeraragavan, A., "Measurements and analysis of hypersonic tripped boundary layer turbulence," *Experiments in Fluids*, Vol. 62, No. 8, 2021. doi:10.1007/s00348-021-03254-z.

[17] Siddiqui, F., Gragston, M., Saric, W. S., and Bowersox, R. D. W., "Mack-mode instabilities on a cooled flared cone with discrete roughness elements at Mach 6," *Experiments in Fluids*, Vol. 62, No. 10, 2021. doi:10.1007/s00348-021-03304-6.

[18] Benitez, E. K., Jewell, J. S., and Schneider, S. P., "Focused Laser Differential Interferometry with Contoured Tunnel Windows," *AIAA Journal*, Vol. 59, No. 2, 2021, pp. 419–429. doi:10.2514/1.j060081.

[19] Yu, T., Xiong, Y., Zhao, J., and Wu, J., "Application of focused laser differential interferometer to hypersonic boundary-layer instability study," *Chinese Journal of Aeronautics*, Vol. 34, No. 5, 2021, pp. 17–26. doi:10.1016/j.cja.2020.10.019.

[20] Davenport, K., and Gragston, M., "Simultaneous Velocity Profile and Scalar Spectra with Linear Array-Focused Laser Differential Interferometry," *AIAA Journal*, Vol. 61, No. 2, 2022, pp. 934–939. doi:10.2514/1.j061945.

[21] Price, T. J., Gragston, M., Schmisseur, J. D., and Kreth, P. A., "Measurement of supersonic jet screech with focused laser differential interferometry," *Applied Optics*, Vol. 59, No. 28, 2020, p. 8902. doi:10.1364/ao.402011.

[22] Gragston, M., Price, T., Davenport, K., Zhang, Z., and Schmisseur, J. D., "Linear array focused-laser differential interferometry for single-shot multi-point flow disturbance measurements," *Optics Letters*, Vol. 46, No. 1, 2021, p. 154. doi:10.1364/ol.412495.

[23] Ceruzzi, A. P., and Cadou, C. P., "Interpreting single-point and two-point focused laser differential interferometry in a turbulent jet," *Experiments in Fluids*, Vol. 63, No. 7, 2022. doi:10.1007/s00348-022-03459-w.

[24] Hameed, A., and Parziale, N. J., "Focused Laser Differential Interferometric Investigation of Turbulent Jet Spectra," *Journal of Spacecraft and Rockets*, Vol. 59, No. 5, 2022, pp. 1565–1573. doi:10.2514/1.a35292.

[25] Schmidt, B. E., and Shepherd, J. E., "Analysis of focused laser differential interferometry," *Applied Optics*, Vol. 54, No. 28, 2015, pp. 8459–8472. doi:10.1364/ao.54.008459.

[26] Settles, G. S., and Fulghum, M. R., "The Focusing Laser Differential Interferometer, an Instrument for Localized Turbulence Measurements in Refractive Flows," *Journal of Fluids Engineering*, Vol. 138, No. 10, 2016, pp. 101402–1–101402–10. doi:10.1115/1.4033960.

[27] Camillo, G. P., and Wagner, A., "Focused laser differential interferometry post-processing methodology for flowfields with circular symmetry," *Review of Scientific Instruments*, Vol. 94, No. 4, 2023, p. 045102. doi:10.1063/5.0132874.

[28] Jiang, N., Hsu, P. S., Gragston, M., and Roy, S., "Recent progress in high-speed laser diagnostics for hypersonic flows [Invited]," *Applied Optics*, Vol. 62, No. 6, 2023, p. A59. doi:10.1364/ao.480298.

[29] Benitez, E. K., Borg, M. P., Rhodes, C., and Jewell, J. S., "Optical-Axis Spatial Sensitivity of a Simulated Focused Laser Differential Interferometer," *AIAA Journal*, Vol. 61, No. 5, 2023, pp. 1925–1938. doi:10.2514/1.j062270.

[30] Lawson, J. M., and Austin, J. M., "Recovering density disturbance spectra from FLDI. Part 1," *Applied Optics*, Vol. 62, No. 12, 2023, p. 3042. doi:10.1364/ao.480352.

[31] Lawson, J. M., and Austin, J. M., "Recovering density disturbance spectra from FLDI. Part 2: comparisons with previous methods," *Applied Optics*, Vol. 62, No. 12, 2023, p. 3054. doi:10.1364/ao.480354.

[32] Lackner, M., "Tunable Diode Laser Absorption Spectroscopy TDLAS in the Process Industries – A Review," *Reviews in Chemical Engineering*, Vol. 23, No. 2, 2007. doi:10.1515/revce.2007.23.2.65.

[33] Bolshov, M. A., Kuritsyn, Y. A., and Romanovskii, Y. V., "Tunable diode laser spectroscopy as a technique for combustion diagnostics," *Spectrochimica Acta Part B: Atomic Spectroscopy*, Vol. 106, 2015, pp. 45–66. doi:10.1016/j.sab.2015.01.010.

[34] Kroll, M., McClintock, J. A., and Ollinger, O., "Measurement of gaseous oxygen using diode laser spectroscopy," *Applied Physics Letters*, Vol. 51, No. 18, 1987, pp. 1465–1467. doi:10.1063/1.98999.

[35] Ritter, K. J., and Wilkerson, T. D., "High-resolution spectroscopy of the oxygen A band," *Journal of Molecular Spectroscopy*, Vol. 121, No. 1, 1987, pp. 1–19. doi:10.1016/0022-2852(87)90167-6.

[36] Bruce, D. M., and Cassidy, D. T., "Detection of oxygen using short external cavity GaAs semiconductor diode lasers," *Applied Optics*, Vol. 29, No. 9, 1990, p. 1327. doi:10.1364/ao.29.001327.

[37] Greenblatt, G. D., Orlando, J. J., Burkholder, J. B., and Ravishankara, A. R., "Absorption measurements of oxygen between 330 and 1140 nm," *Journal of Geophysical Research*, Vol. 95, No. D11, 1990, p. 18577. doi:10.1029/jd095id11p18577.

[38] Philippe, L. C., and Hanson, R. K., "Laser diode wavelength-modulation spectroscopy for simultaneous measurement of temperature, pressure, and velocity in shock-heated oxygen flows," *Applied Optics*, Vol. 32, No. 30, 1993, p. 6090. doi:10.1364/ao.32.006090.

[39] Dharamsi, A. N., and Lu, Y., "Sensitive density-fluctuation measurements using wavelength-modulation spectroscopy with high-order-harmonic detection," *Applied Physics B Laser and Optics*, Vol. 62, No. 3, 1996, pp. 273–278. doi:10.1007/bf01080955.

[40] Gianfrani, L., Sasso, A., and Tino, G. M., "Monitoring of O2 and NO2 using tunable diode lasers in the near-infrared region," *Sensors and Actuators B: Chemical*, Vol. 39, No. 1-3, 1997, pp. 283–285. doi:10.1016/s0925-4005(97)80219-5.

[41] Benedetti, R., Giulietti, K., and Rosa-Clot, M., "Line shape analysis of O_2 in air as a way to measure temperature using a DFB-diode-laser at 761 nm," *Optics Communications*, Vol. 154, No. 1-3, 1998, pp. 47–53. doi:10.1016/s0030-4018(98)00258-2.

[42] Brown, L. R., and Plymate, C., "Experimental Line Parameters of the Oxygen A Band at 760 nm," *Journal of Molecular Spectroscopy*, Vol. 199, No. 2, 2000, pp. 166–179. doi:10.1006/jmsp.1999.8012.

[43] Sanders, S. T., Wang, J., Jeffries, J. B., and Hanson, R. K., "Diode-laser absorption sensor for line-of-sight gas temperature distributions," *Applied Optics*, Vol. 40, No. 24, 2001, p. 4404. doi:10.1364/ao.40.004404.

[44] Vogel, P., and Ebert, V., "Near shot noise detection of oxygen in the A-band with vertical-cavity surface-emitting lasers," *Applied Physics B*, Vol. 72, No. 1, 2001, pp. 127–135. doi:10.1007/s003400000516.

[45] Wang, J., Sanders, S. T., Jeffries, J. B., and Hanson, R. K., "Oxygen measurements at high pressures with vertical cavity surface-emitting lasers," *Applied Physics B*, Vol. 72, No. 7, 2001, pp. 865–872. doi:10.1007/s003400100539.

[46] Tran, H., Boulet, C., and Hartmann, J.-M., "Line mixing and collision-induced absorption by oxygen in the A band: Laboratory measurements, model, and tools for atmospheric spectra computations," *Journal of Geophysical Research*, Vol. 111, No. D15, 2006. doi:10.1029/2005jd006869.

[47] Hamilton, M. L., Ritchie, G. A. D., Arita, Y., and Ewart, P., "Multi-mode absorption spectroscopy, MUMAS, using wavelength modulation and cavity enhancement techniques," *Applied Physics B*, Vol. 100, No. 3, 2010, pp. 665–673. doi:10.1007/s00340-010-4040-8.

[48] Zhang, Z.-R., Sun, P.-S., Xia, H., Li, Z., Pang, T., Wu, B., Cui, X.-J., and Dong, F.-Z., "Detection of gas temperature using a distributed feedback laser at O_2 absorption wavelength 760 nm," *Journal of Optical Technology*, Vol. 83, No. 11, 2016, p. 673. doi:10.1364/jot.83.000673.

[49] Jatana, G. S., Perfetto, A. K., Geckler, S. C., and Partridge, W. P., "Absorption spectroscopy based high-speed oxygen concentration measurements at elevated gas temperatures," *Sensors and Actuators B: Chemical*, Vol. 293, 2019, pp. 173–182. doi:10.1016/j.snb.2019.04.143.

[50] Vasilchenko, S., Mikhailenko, S. N., and Campargue, A., "Water vapor absorption in the region of the oxygen A-band near 760 nm," *Journal of Quantitative Spectroscopy and Radiative Transfer*, Vol. 275, 2021, p. 107847. doi:10.1016/j.jqsrt.2021.107847.

[51] Sun, K., Chao, X., Sur, R., Goldenstein, C. S., Jeffries, J. B., and Hanson, R. K., "Analysis of calibration-free wavelength-scanned wavelength modulation spectroscopy for practical gas sensing using tunable diode lasers," *Measurement Science and Technology*, Vol. 24, No. 12, 2013, p. 125203. doi:10.1088/0957-0233/24/12/125203.

[52] Weisberger, J. M., Herring, G. C., Bathel, B. F., and Chou, A., "Absorption Laser Differential Interferometer for Simultaneous Colinear Flow Property and Fluctuation Measurements," *AIAA AVIATION 2023 Forum*, 2023.

[53] Berger, K. T., Hollingsworth, K. E., Wright, S. A., and Rufer, S. J., "NASA Langley Aerothermodynamics Laboratory: Hypersonic Testing Capabilities," *53rd AIAA Aerospace Sciences Meeting*, AIAA-2015-1337, 2015. doi:10.2514/6.2015-1337.